Available online at www.sciencedirect.com
SCIENCE DIRECT®
Journal of Nuclear Materials 326 (2004) 38–46
journal of nuclear materials
www.elsevier.com/locate/jnucmat

Microstructural characteristics and embrittlement phenomena in neutron irradiated 309L stainless steel RPV clad

J.S. Lee [a], I.S. Kim [a,*], R. Kasada [b], A. Kimura [b]

[a] Department of Nuclear and Quantum Engineering, KAIST, 373-1 Guseong-dong, Yuseong-gu, Daejeon 305-701, South Korea
[b] Institute of Advanced Energy, Kyoto University, Gokasho, Uji, Kyoto 611-0011, Japan

Received 9 February 2003; accepted 23 November 2003

Abstract

The effects of neutron irradiation on the microstructural features and mechanical properties of 309L stainless steel RPV clad were investigated using TEM, SEM, small tensile, microhardness and small punch (SP) tests. The neutron irradiations were performed at 290 °C up to the fluences of 5.1×10^{18} and 1.02×10^{19} n/cm^2 (>1 MeV) in Japan Materials Testing Reactor (JMTR). The microstructure of the clad before and after irradiation was composed of main part of fcc austenite, a few percent of bcc δ-ferrite and small amount of brittle σ phase. After irradiation, not only the yield stress and microhardness, but SP ductile to brittle transition temperature (SP-DBTT) were increased. However, the increase in SP-DBTT is almost saturated, independent of the neutron fluence. Based on the TEM observation, the origin of irradiation hardening was accounted for by the irradiation-produced defect clusters of invisible fine size (<1–2 nm), and the shift of SP-DBTT was primary due to the higher hardening and the preferential failure of δ-ferrite. The embrittlement of the clad was strongly affected by the initial microstructural factors, such as the amount of brittle σ phase, which caused a cracking even in an early stage of deformation.

PACS: 61.80.Hg

1. Introduction

The inner wall of nuclear reactor pressure vessel (RPV) was overlay cladded with 300 grade austenitic stainless steels of a few millimeter thickness to prevent the general corrosion attack of the ferritic low alloy steel and the radioactive contamination problems in main coolant systems. The presence of clad requires additional information on the material properties to assess the RPV safety, and the properties of the clad are considered to be influenced by in-service exposure to the high energy neutron irradiation at the reactor operating temperature. In this regard, understanding the clad properties under neutron irradiation is an important factor for safe and extended service life operation.

As for the nuclear RPV cladding materials, a number of post-irradiation tests using tensile, Charpy impact, and fracture toughness tests have been carried out in several research institutes, and they reported an increase in yield stress, a reduction of fracture toughness (J_{IC}) and a shift of ductile to brittle transition temperature (DBTT) [1–3] depending on specimen sampling position, weld metals, and test temperature etc. However, since those results are mainly focused on the evaluation of mechanical properties with irradiation, it is still insufficient to explain the mechanism of the hardening and embrittlement which is thought to be associated with the microstructural features of the clad.

* Corresponding author. Tel.: +82-42 869 3815; fax: +82-42 869 3810.
E-mail address: iskim@kaist.ac.kr (I.S. Kim).

0022-3115/$ - see front matter © 2003 Elsevier B.V. All rights reserved.
doi:10.1016/j.jnucmat.2003.11.005

In nuclear industry, strip welding with submerged arc or electroslag technique was most common techniques for production of RPV clad, and the microstructure of the clad was composed of a main part of fcc austenite, a few percent bcc δ-ferrite that was produced during overlay welding. Small amount of δ-ferrite is desirable in the weld zones of austenitic stainless steels, because the ferrite phase prevents hot tearing or cracking. On the other hand, the δ-ferrite could cause the thermal aging embrittlement through the decomposition of δ-ferrite to brittle σ phase, new austenite (γ′), and chromium rich carbide ($M_{23}C_6$ type), when it is exposed to the temperature range between 600 and 900 °C [4–6]. Further, the volume fractions of each phase were considerably influenced by the chemical composition of filler metal, cooling rate during overlay welding and distance from the weld fusion line [7,8].

The objectives of this research are to investigate the effect of microstructure of the clad that depends on the heat input rate during submerged arc welding process, and their effects on the hardening and ductile to brittle transition behavior following neutron irradiation by using the results of microhardness, small tensile and small punch (SP) tests.

2. Experimental

The material used was the weld metal of AWS Class ER309L stainless steel that was commonly used in nuclear industry. The chemical compositions of 309L is given in Table 1. The cladding was deposited with submerged arc welding process on SA508 cl.3 plates and two kinds of heat input rates were chosen (Table 2). Heat treatment conditions during overlay welding and postweld heat treatment (PWHT) are shown in Table 3.

The microstructure of the clad were examined using scanning electron microscope (SEM) after electrolytic etching in a solution of 50 g NaOH in 100 ml water at 2 V for 5 s, and thin foils for transmission electron microscopy (TEM) were fabricated by twin jet electropolishing in a solution of 10% perchloric acid + 90% ethanol at −30 °C. The ferrite content was measured using a Ferrite Content Meter, and the fraction of σ phase in the clad was measured by image analyzer after electrolytic etching (Table 2).

The small size tensile (gage length = 5 mm, $1.2^{w} \times 0.28^{t}$ mm) and TEM disk ($3\phi \times 0.28^{t}$ mm) type small punch (SP) specimens were sampled from 2 mm away from the weld fusion line to avoid a dilution effect between the clad and the RPV steel. Tensile tests and SP tests were performed at a cross-head speed of 0.2 mm/min. at room temperature and temperatures from ~77 to 293 K, respectively. One millimeter diameter steel balls with Rockwell hardness (HRC) of over 60 were employed for loading fixtures. Specific SP energy was determined by the area under load–deflection curve per unit thickness of the given specimen, and SP ductile to brittle transition temperature (SP-DBTT) was defined as a temperature where the specific SP energy was the average of maximum specific SP energy and lower shelf energy. Following SP tests, fracture appearance was observed by a SEM to identify the cracking path of the specimen at different test temperatures.

Tensile and SP specimens were neutron irradiated in the Japan Materials Testing Reactor (JMTR) at 290 ± 1 °C. The irradiation fluences were 5.1×10^{18} and 1.02×10^{19} n/cm^2 (>1 MeV), which corresponded to approximately 0.009 and 0.018 dpa, respectively.

Electrical resistivity was measured with a conventional four probe direct current bridge on small tensile specimens at liquid nitrogen temperature and average values of 10 measurements were used. Vickers microhardness test was carried out with a 10 g load at room temperature.

Table 2
The maximum heat input rate and volumetric phase fractions (%) of RPV clad

Index	Max. heat input rate (kJ/cm)	δ-ferrite (FN[a]) (before PWHT)	δ-ferrite (FN) (After PWHT)	σ phase[b]
K001	164.4	9.1	6.6	1.9
K002J	188.5	10.2	2.5	7.9

[a] FN: ferrite number was measured by Ferrite Content Meter, which almost equals to the volumetric percentage.

[b] The fraction of σ phase was determined by image analyzer after electrolytic etching in a solution of 50 g NaOH + 100 ml water.

Table 3
Heat treatment conditions during overlay welding and postweld heat treatment

Preheating	121 °C min.
Inter-pass heating	176 °C max.
Posting heating	210–310 °C/2 h
Postweld heat treatment (PWHT)	620–628 °C/41 h

Table 1
The chemical composition of AWS Class ER309L weld metal (w/o)

C	Si	Mn	P	S	Cr	Ni	Mo	Co	V	Ti	Cu	Nb	N
0.011	0.36	1.60	0.013	0.001	23.77	13.19	0.06	0.026	0.052	0.09	0.039	<0.01	0.045

3. Results

3.1. SP properties and fracture appearance

The effects of neutron irradiation on the SP-DBTT of both the specimens are shown in Fig. 1. In unirradiated condition, K001 clad showed a small increase in SP energy with decreasing temperature up to a maximum energy at around 183 K. As the test temperature decreased further, a sudden drop of SP energy was observed showing ductile to brittle transition, and the SP-DBTT was shifted to a higher temperature by the irradiation.

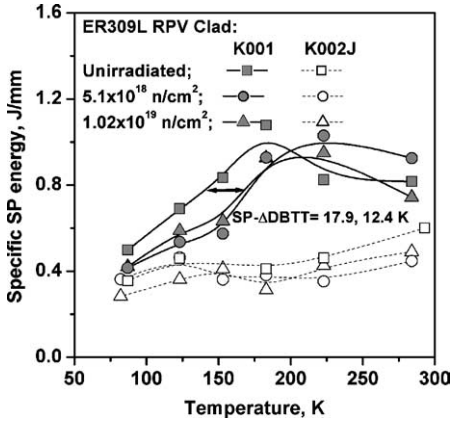

Fig. 1. The variations of specific SP energy of each clad as a function of neutron fluence and test temperature.

The SP-DBTT in unirradiated K001 clad was 144 K and the increase in SP-DBTT (SP-ΔDBTT) is almost similar independent of the neutron fluence, suggesting that the irradiation embrittlement appears to be saturated at 1×10^{19} n/cm^2 (>1 MeV). When the SP-ΔDBTT, which were 17.9 and 12.4 K for 5.1×10^{18} and 1.02×10^{19} n/cm^2, respectively, were converted to the standard CVN-ΔDBTT impact test using the empirical relationship between SP and CVN impact test [9], it resulted in the CVN-ΔDBTT of 31–45 K, similar to other researchers' results [3].

On the contrary, the K002J clad did not show a transition behavior of SP energy, basically the specific SP energy showed ground energy levels irrespective of test temperatures and neutron doses. Such a brittle behavior of K002J may be related with its microstructural characteristics, especially with the existence of brittle of σ phase [10].

Fracture surface observation following SP tests revealed that the dominant fracture mode of K001 specimens was brittle transgranular type at temperatures below 183 K as shown in Fig. 2, while the fracture mode was ductile above 183 K. Fig. 2(a) appears to show intergranular fracture. However, the observation with higher magnification clearly shows the fracture mode is quasi-cleavage. This indicates that the fracture occurred in the δ-ferrite phases which are formed along austenitic grain boundaries. In the mean time, significant cracking of σ phase was observed in K002J specimens as shown in Fig. 2(c) and (d) at both the temperature of (c) 293 K and (d) 87 K.

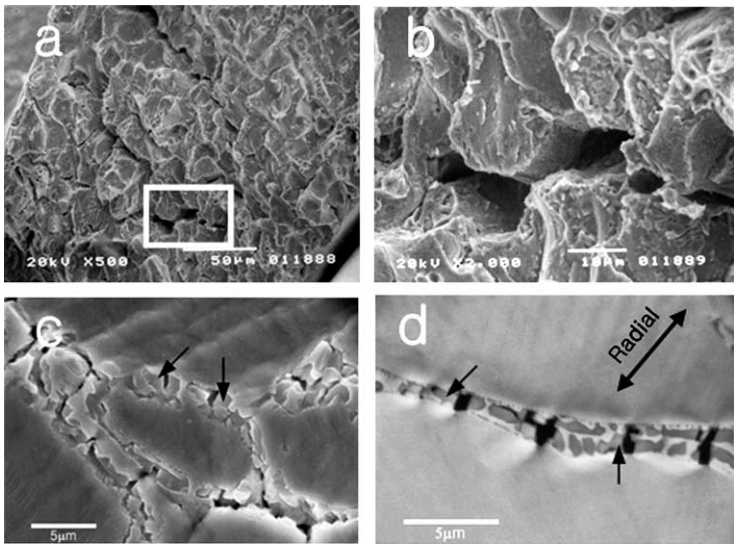

Fig. 2. Scanning electron micrographs of cracking appearance of RPV clad: (a) represents through-thickness fracture surface of irradiated K001 SP specimen tested at 77 K, fluence = 1.02×10^{19} n/cm^2. (b) is higher magnification of the region indicated in (a). Cracking of σ phase in unirradiated K002J SP specimen tested at (c) 293 K and (d) 87 K. Arrows in (c) and (d) indicate the cracking of phase during SP deformation process.

3.2. Micro-Vickers hardness measurement

The irradiation hardening of δ-ferrite and austenitic phase was evaluated by means of micro-Vickers hardness measurements. Since the size of indenter at 10 g load was larger than that of δ-ferrite, the measured values at δ-ferrite phase were influenced by surrounding austenite phases. However, the obtained results indicate that a significant difference in the hardness exists between δ-ferrite and austenite phase, as shown in Fig. 3, where rectangles are the hardness measured with the indenter located on the δ-ferrite + γ austenite phase ($\delta+\gamma$), and the circles are those when the indenter was located in the austenite phase. In both the cases, irradiation hardening was observed and the hardening increased with increasing neutron fluences. It is worth to note that the irradiation hardening was more significant for ($\delta+\gamma$) than γ-phase, suggesting that the δ-ferrite phase is more highly susceptible to irradiation hardening. The difference of Hv between $\delta+\gamma$ and γ alone was 14 at unirradiated condition. After irradiation, the Hv in $\delta+\gamma$ and in γ gradually increased and the difference of Hv between them was about 30, irrespective of neutron fluence. To compare the irradiation-induced hardening between δ-ferrite and austenite, the hardness value of δ-ferrite was estimated by decomposing the Hv ($\delta+\gamma$) Gaussian distribution curve into each Hv Gaussian curve, namely, Hv Gaussian distribution curve of a δ-ferrite and of a γ austenite. Detailed implementation of the method is reported in Ref. [11]. It is considered that the δ-ferrite was hardened from 235 to 266 at 5.1×10^{18} and to 290 at 1.02×10^{19} n/cm^2. Meanwhile Hv of γ increased from 216 to 236 and to 252 depending on the fluence. This results revealed that the hardening ability of δ-ferrite by neutron irradiation ($\Delta Hv_\delta/\Delta Hv_\gamma$) was 1.5 times higher than the austenite matrix. Similar results were also reported in type 304 stainless steel weldment by utilizing an ion irradiation [11].

3.3. Tensile properties

Fig. 4 shows the dependence of tensile strength and ductility at room temperature on neutron fluence. The K002J clad showed a higher yield stress (σ_y) than the K001 in unirradiated condition and the difference was about 24 MPa. After irradiation, the σ_y was increased in both samples. The increment of yield stress ($\Delta\sigma_y$) was about 66 at 5.1×10^{18} and 84 MPa at 1.02×10^{19} n/cm^2 (>1 MeV) in K001 clad, while the $\Delta\sigma_y$ in K002J was about 45 and 40 MPa, respectively. The higher yield stress in unirradiated K002J specimen was thought to be resulted from the larger fraction of hard σ phase (~7.9%), and the irradiation hardening was due to the complex effect on both the δ-ferrite and γ austenite, although the clad was composed of ~90% austenite phase.

Tensile strength (σ_{uts}) of K001 did not show any hardening effects by the irradiation. This is due to irradiation-induced reduction of fracture stress that suppresses work-hardening. In case of K001 clad, the σ_{uts} was about 500 MPa before and after irradiation, while the σ_{uts} in K002J was 522 MPa in unirradiated condition and reduced to 487 and 457 MPa according to the fluence.

As for the ductility change, neutron irradiation reduced the elongation. After irradiation the plastic fracture strain (ε_f) in K001 clad was reduced to 76% and 67% compared to the unirradiated one. However, the ductility of K002J was much smaller than that of K001 even at unirradiatied condition showing about 56%, and reduced to 43% and 42% by the irradiations. It is worth

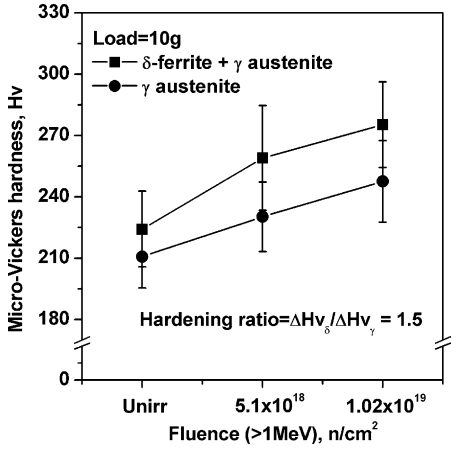

Fig. 3. The comparison of micro-Vickers hardness between δ-ferrite plus austenite and γ austenite matrix with neutron irradiation.

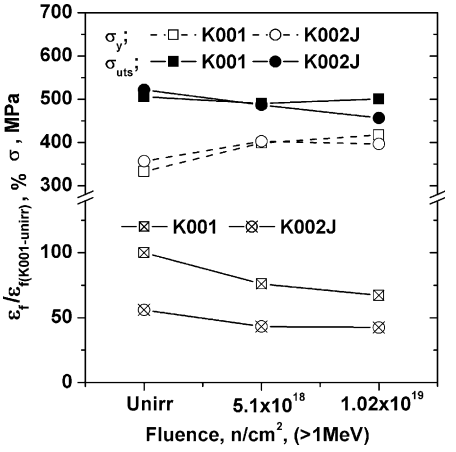

Fig. 4. The variations of tensile properties, such as yield stress (σ_y), tensile strength (σ_{uts}) and fracture strain (ε_f), as a function of neutron fluence.

to notice that the ductility of K002J at unirradiated condition was still lower than that of irradiated K001 clad.

3.4. Electrical resistivity measurement

In metal, as the changes in resistivity, $\Delta\rho$, is generally proportional to the concentration of irradiation-produced defects [12,13], it is often used to detect the formation of irradiation defects. Fig. 5 presents the results of the electrical resistivity measurement at 77 K, indicating that the electrical resistivity ($\Delta\rho$) was increased with neutron fluence in both samples. It is reasonable to assume that those mainly represent the resistivity of austenite phase because the volume fraction of the austenite phase is about 90% in the clad.

3.5. Microstructural features

Fig. 6 presents typical microstructure of 309L clad varying with the heat input rate during submerged arc welding, indicating that both the clads were composed of about 90% fcc austenite, a few percent of bcc δ-ferrite and brittle σ phase. The δ-ferrite was mainly formed at the austenite grain boundaries. As listed in Table 2, the higher heat input prior to PWHT (K002J sample) resulted in a slightly larger fraction of δ-ferrite than the lower one (K001 sample).

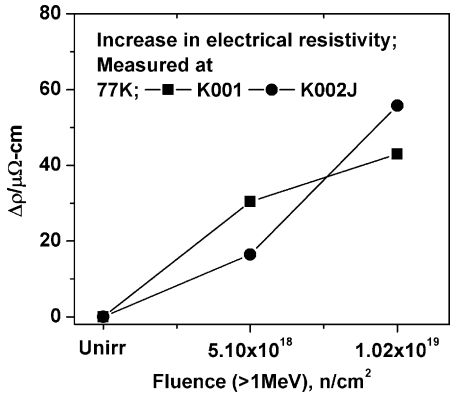

Fig. 5. The electrical resistivity changes in each clad as a function of neutron fluence.

Fig. 7 shows the microstructural features of the clads, especially inside of δ-ferrite after applying the PWHT. Since we used a backscattered electron (BSE) detector for SEM observation, σ phase, which contained high percentage of chromium [6], represented as dark color compared to the δ-ferrite and γ austenite. Images produced by BSE show characteristic atomic number contrast, that is, features of high atomic number (Z) appear brighter than those of low Z. In K002J clad, the initial δ/γ boundaries moved into the δ-ferrite and the remaining was almost transformed to σ and new austenite (γ') during PWHT. In the mean time the formation of σ in K001 clad was not significant.

3.6. TEM observations

The typical TEM microstructure of the irradiated K001 sample is shown in Fig. 8(a). Analysis of the diffraction patterns of the grain A and B revealed that the grain A and B has a fcc and bcc structure with the lattice parameter of 0.360 nm and 0.284 nm, respectively, as expected for austenitic phase (γ) and δ-ferrite phase. The characteristic features in the δ-ferrite phase is the carbide precipitation. Fig. 8(c) is the diffraction pattern of the carbides shown in Fig. 8(b), indicating that the carbides are $M_{23}C_6$ type with the lattice parameter of 1.08 nm. Fig. 8(d) and (e) is the bright and dark field images of the carbides taken by an extra spot of $M_{23}C_6$ carbides. It is confirmed that the K001 sample consists of γ phase and δ-ferrite phase as well as $M_{23}C_6$ type carbides precipitated at the γ/δ phase boundaries.

In contrast, the K002J sample consists of γ- and δ-ferrite (or γ' phase) as well as σ phase, as shown in Fig. 9(a) with the diffraction patterns of them. The diffraction patterns of grain A, B, C and D in Fig. 9(a) are shown in Fig. 9(b), (c), (d) and (e), respectively. Consequently, it is considered that the δ-ferrite phase formed by welding transformed into γ' phase and σ phase during PWHT.

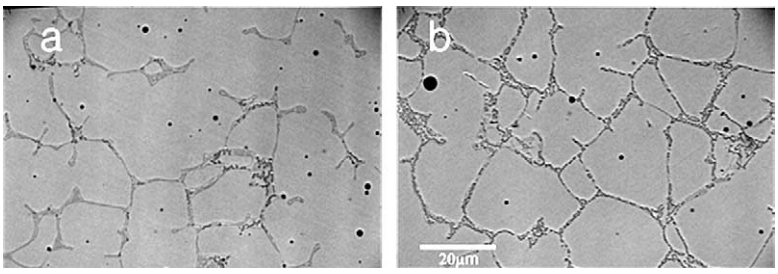

Fig. 6. Scanning electron micrographs of RPV clad, gray = austenite, dark gray = δ-ferrite plus σ phase, backscattered electron (BSE) mode: (a) K001, (b) K002J.

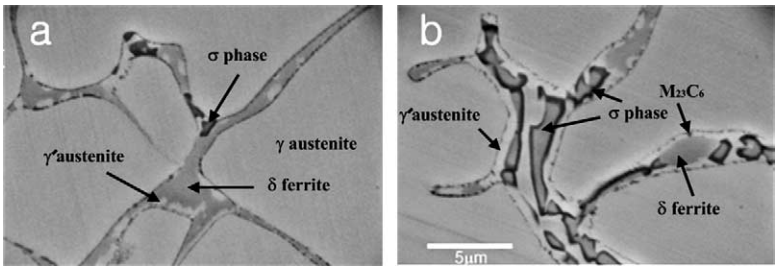

Fig. 7. Typical microstructural characteristics of inside of δ-ferrite, gray = austenite, white gray = new austenite (γ′), dark gray = δ-ferrite, black = σ phase, backscattered electron (BSE) mode: (a) K001, (b) K002J.

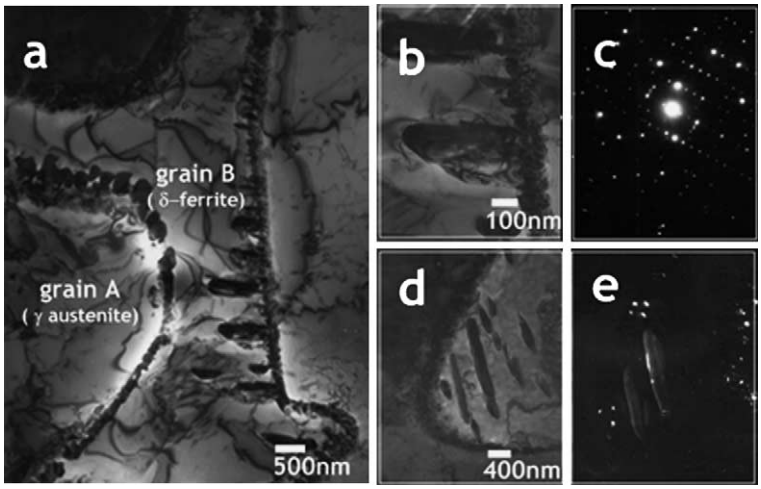

Fig. 8. Transmission electron micrographs of neutron irradiated K001 clad, showing (a) typical microstructure, (b) $M_{23}C_6$ type carbides precipitation, (c) diffraction pattern of the carbides shown in (b), (d) and (e) is the bright and dark field images of the carbides taken by an extra spot of $M_{23}C_6$ carbides.

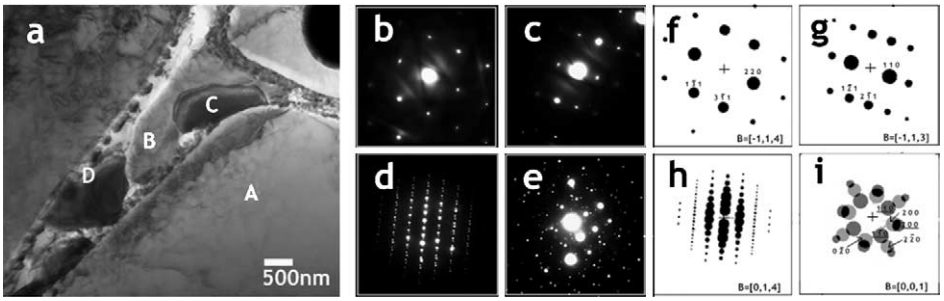

Fig. 9. Transmission electron micrographs of neutron irradiated K002J clad, showing (a) typical microstructure. The diffraction patterns of grain A (γ), B (δ), C (σ) and D (δ + γ′) in (a) are shown in (b), (c), (d) and (e), respectively. (f), (g), (h) and (i) is computer simulated selected area diffraction patterns of fcc γ, bcc δ, bct σ and γ + δ, respectively (underbar marks in (i) indicate the indices of δ-ferrite), Fluence = 1.02×10^{19} n/cm^2 (>1 MeV).

The phases were often observed by TEM in K002J but scarcely observed in K001 sample.

Fig. 10 shows the TEM micrographs of δ-ferrite phase (Fig. 10(a)), γ-phase (Fig. 10(b)) and σ-phase (Fig. 10(c)) taken with a relatively high magnification. Although both the δ-ferrite and γ phases were hardened by neutron irradiations, any visible defect clusters were not observed in those phases, suggesting that the defect

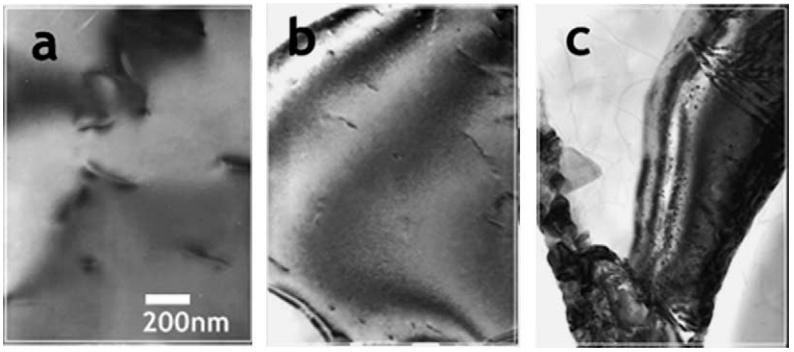

Fig. 10. Transmission electron micrographs of (a) δ-ferrite phase, (b) γ phase and (c) σ phase taken with a relatively high magnification, fluence = 1.02×10^{19} n/cm^2 (>1 MeV).

clusters contributing the irradiation hardening are too small to be observed by TEM, namely smaller than 1 nm. On the other hand, many small dot like structures were observed in the σ-phase (Fig. 10(c)). It is difficult to identify the characteristics of the dot like structure, but they may be the small dislocation loops formed in the σ-phase.

4. Discussion

4.1. Microstructural characteristics

The different amount of σ phase precipitation between the clads is considered to be due to the different cooling rate resulted from the different heat input rates during overlay welding. Since K002J sample was fabricated with high heat input rate, it might result in a slower cooling rate than that of K001 sample. It was reported that the amount of σ phase was increased at a slow cooling rate [7]: if cooling rate was decreased from 0.25 to 0.1 °C s^{-1} for the 2205 duplex stainless steel weldment, the volume fraction of σ phase precipitation was increased from $0+1$ to 7.8 ± 1 vol.%. And, also another possibility is the difference of total available chromium atoms in δ-ferrite phase. The chromium atoms are consumed to form a σ phase during PWHT [5,6]. Since the chromium is the stabilizer of ferrite phase, the δ-ferrite can posses higher chromium compared with the austenite phase. Further, before PWHT the volume fraction of δ-ferrite in K002J clad were larger than those in K001, the total amount of available chromium in K002J clad was larger than K001. Accordingly, K002J clad had a higher potential to form the σ phase, and resulted in the larger fraction of σ in K002J clad rather than in K001 (Table 2).

The PWHT on the clad resulted in a reduction of δ-ferrite content and that is interpreted in terms of the decomposition of δ-ferrite to new austenite (γ'), chromium rich carbide ($M_{23}C_6$ type) and σ phase during the heat treatment [4–6]. The decomposition of δ-ferrite during PWHT may proceed through by the following two reaction mechanisms. At first, it is considered that the precipitation of chromium rich carbides occur at initial δ/γ boundaries by the eutectoid reaction ($\delta \rightarrow M_{23}C_6 + \gamma'$), and evoked the movement of δ/γ boundaries into the δ-ferrite. Then, the formation of σ and new austenite (γ') ($\delta \rightarrow \sigma + \gamma'$) occurs. The σ phase is a hard intermetallic phase with a complex tetragonal structure, which often causes the degradation of mechanical properties [6,10].

On the other hand, if high energy neutrons were irradiated to austenitic stainless steels, they will create defects such as vacancy/interstitial (V/I) clusters, stacking faults tetrahedra (SFT), loops, and voids depending on dose, dose rate, irradiation temperature, and so on [14–18]. But, the present TEM observations could not reveal any discernable irradiation-produced defects inside of δ and austenite phase. These were thought to be related with the lack of TEM resolution and relatively lower neutron dose in current test [19]. Considering the results of electrical resistivity, tensile, and microhardness measurements, however, there must be fine size defect clusters formed both in δ and in austenite phase.

4.2. Ductile to brittle transition behavior

The transition behavior of specific SP energy in K001 was obviously induced by the preferential failure of δ-ferrite at low temperatures because mechanical properties of ferritic phase were inherently sensitive to test temperature. As shown in Fig. 11, during the SP test at low temperatures the microcracks were formed due to the selective fracture of δ-ferrite along the austenite grain boundaries by the application of high radial and circumferential stress [20]. Thus, the cracking appearance appears to be an intergranular type, but actually it was quasi-cleavage fracture. At the same time the irradiation induced shift of SP-DBTT was considered to be originated from the irradiation hardening of δ-ferrite.

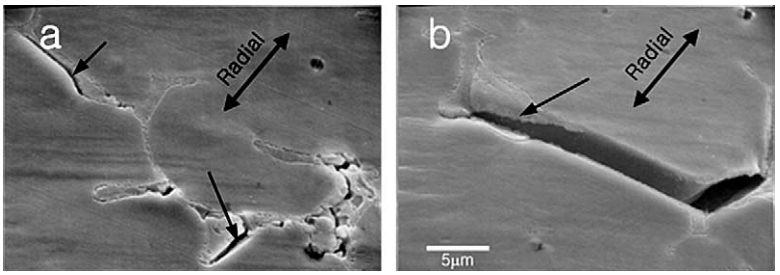

Fig. 11. Preferential failure of δ-ferrite in unirradiated K001 SP specimen tested at 87 K: (a) and (b) represents the phase separation between δ and γ, and fracture of δ-ferrite, respectively.

According to our recent stress analysis results, the fracture stress of ferritic phase, approximately 1000 MPa [21], would be attained when the unirradiated K001 SP specimen was deflected about 0.1 mm at 77 K [22]. Since neutron irradiation induced a higher hardening in δ-ferrite than in austenite phase, the critical deflection to cause the fracture of ferritic phase, must be reduced. Consequently, the total absorbed energy to the final fracture of SP specimens was reduced to shift the SP-DBTT.

On the contrary, ductile to brittle transition behavior of K002J was disappeared even at unirradiated condition, showing ground energy levels irrespective of temperatures and neutron irradiation. The fracture strain of unirradiated K002J showed much lower value than that of irradiated K001 clad, as shown in Fig. 4. This is attributed to the significant cracking of σ phase at an early stage in the deformation process of K002J that contains larger volume fraction of σ phase (~7.9%). The σ phase tended to fracture rather than plastically deformed during deformation and its fracture stress was known as 750 MPa [10]. During SP test, cracking of phase will be started when the peak stress at the SP specimen was equal to the fracture stress of σ phase. According to the stress analysis results, this occurred at a relatively small deflection even in unirradiated condition, approximately 0.26 and 0.03 mm at 293 and 87 K, respectively [22]. Hence, the cracked σ phase at an early stage in deformation process acted as a nucleation site of the fracture, and consequently induced an earlier failure of the specimen. Thus, the lower SP energy would be unavoidable, regardless of irradiation. In the present works, we noticed that the embrittlement of RPV clad was much significantly controlled by the initial microstructural factors, such as the amount of brittle σ phase.

4.3. Irradiation-induced hardening

Although irradiation-induced defects and/or precipitates were not observed in current tests in both the δ-ferrite and austenite phase, the formation of the defects was reflected by the results of microhardness test. As shown in Fig. 3, the microhardness of δ-ferrite and γ austenite were increased by the irradiation, and the hardening ability of δ-ferrite by the irradiation ($\Delta Hv_\delta/\Delta Hv_\gamma$) was 1.5 times higher than the austenite matrix. The higher hardening ability of bcc δ-ferrite than that of fcc austenite is interesting since there is an apparent difference in the accumulation rate of defect clusters. Bcc Fe showed a smaller defect accumulation rate compared with that of fcc Cu and Ni, and three orders of magnitude higher doses would be necessary to reach the same defect density [14]. These were, however, corresponded to the accumulation and growth rate of visible larger size defect density. The computer simulations of the cascade and defect microstructure evolution indicated that although the visible defect density in fcc Cu was much larger than in bcc Fe, the total defect density both in Fe and in Cu was similar [23], when the invisible fine size defect clusters are involved, and most of the defect type in bcc Fe wasI-clusters [24–26].

The presence of the defects, interstitial (I) and vacancy (V) type clusters, in γ austenite was suggested by the result of resistivity measurement. In metal, the change of resistivity, $\Delta\rho$, is generally proportional to the concentration of irradiation-produced defects, C; $\Delta\rho \approx \rho_I C_I + \rho_V C_V - \rho_S C_S$ where ρ_I, ρ_V and ρ_S is the resistivity of unit concentration of Is, Vs and precipitates, respectively [12,13]. For that reason, when the I- and/or V-type clusters were produced, the $\Delta\rho$ would increase according to the defect number densities. In the meantime, as shown in Fig. 5, the resistivity was increased after irradiation, it suggested the formation of invisible fine size of defect clusters (<1–2 nm) and increment of the clusters with fluence in γ austenite phase. However, the possibility of formation of fine size precipitates in the austenite phase is low, because if those were formed, the electrical resistivity might be reduced, instead of increment in current results.

5. Conclusions

The microstructural characteristics of type ER309L RPV clad and their related effect to the hardening and

transition temperature behavior with neutron irradiation were investigated. The main results were as follows:

1. The microstructure of the clad was composed of a main portion of fcc austenite and a few percent of bcc δ-ferrite, and the transformation of δ-ferrite during postweld heat treatment resulted in the formation of $M_{23}C_6$ type carbides at the initial δ/γ grain boundaries and brittle σ phase.
2. The shift of SP ductile to brittle transition temperature (SP-DBTT) in K001 clad by neutron irradiation may come from the higher hardening ability as well as preferential failure of δ-ferrite at low temperature. The embrittlement of RPV clad was strongly affected by the initial microstructural factors, such as the amount of brittle σ phase, which caused a cracking even in an early stage of deformation.
3. The general hardening may come from the irradiation-produced fine size defect clusters in the γ austenite matrix, however the δ-ferrite showed about 1.5 times higher irradiation hardening ability than the austenite matrix.

Acknowledgements

This work has been carried out as a part of the Core University Program (CUP) between Korea and Japan, supported by Ministry of Science and Technology (MOST) in Korea and Japan Society for the Promotion of Science (JSPS). The authors are grateful to DooSan Heavy Industry for supplying of RPV clad materials and the staff of Oarai branch, Institute for Materials Research (IMR), Tohoku University for their help.

References

[1] M.G. Hortsten, W.P.A. Belcher, in: S.T. Rosinski et al. (Eds.), 20th International Symposium, ASTM STP 1405, ASTM, West Conshohocken, 2001, p. 328.
[2] F.M. Haggag, in: A.S. Kumar et al. (Eds.), 16th International Symposium, ASTM STP 1175, ASTM, Philadelphia, 1993, p. 363.
[3] F.M. Haggag, W.R. Corwin, R.K. Nanstard, Nucl. Eng. Des. 124 (1990) 129.
[4] J.A. Brooks, A.W. Thompson, Inter. Mater. Rev. 36 (1) (1991) 16.
[5] K.M. Lee, H.S. Cho, D.C. Choi, J. Alloys Compd. 285 (1999) 156.
[6] C.C. Tseng, Y. Shen, S.W. Thompson, M.C. Mataya, G. Krauss, Metall. Mater. Trans. A 25A (1994) 1147.
[7] L.H. Chiu, W.C. Hsieh, C.H. Wu, Mater. Sci. Eng. A 354 (2003) 82.
[8] J.F. Lancaster, Metallurgy of Welding, Chapman and Hall, UK, 1993, p. 266.
[9] R. Kasada, T. Morimura, A. Hasegawa, A. Kimura, J. Nucl. Mater. 299 (2001) 83.
[10] A.V. Kington, F.W. Noble, Mater. Sci. Eng. A 138 (1991) 259.
[11] S.H. Chi, Y.K. Shin, G.C. Kim, Y.J. Kim, J.H. Hong, Mater. Trans. 43 (4) (2002) 1.
[12] Y. Chimi, A. Iwase, N. Ishikawa, J. Nucl. Mater. 271&272 (1999) 236.
[13] J.W. Martin, J. Phys. F: Metal Phys. 2 (1972) 842.
[14] M. Victoria, N. Baluc, C. Bailat, Y. Dai, M.I. Luppo, R. Schaublin, B.N. Singh, J. Nucl. Mater. 276 (2000) 114.
[15] N. Hashimoto, E. Wakai, J.P. Robertson, J. Nucl. Mater. 273 (1999) 95.
[16] J. Gan, G.S. Was, J. Nucl. Mater. 297 (2001) 161.
[17] M. Horiki, M. Kiritani, J. Nucl. Mater. 212–215 (1994) 246.
[18] H. Watanabe, T. Muroga, N. Yoshida, J. Nucl. Mater. 271&272 (1999) 381.
[19] W.J. Mills, Inter. Mater. Rev. 42 (2) (1997) 45.
[20] J.S. Cheon, I.S. Kim, J. Nucl. Mater. 278 (2000) 96.
[21] G.E. Dieter, Mechanical Metallergy, 2nd Ed., McGraw-Hill, 1976, p. 367.
[22] J.S. Lee, I.S. Kim, A. Kimura, J. Nucl. Sci. Technol. 40 (9) (2003) 664.
[23] M.J. Caturla, N. Soneda, E. Alonso, B.D. Wirth, T. Dıaz de la Rubia, J.M. Perlado, J. Nucl. Mater. 276 (2000) 13.
[24] B.L. Eyre, A.F. Bartlett, Philos. Mag. 12 (1965) 261.
[25] R. Kasada, A. Kimura, J. Nucl. Mater. 283–287 (2000) 188.
[26] W.J. Phythian, R.E. Stoller, A.J.E. Foreman, A.F. Calder, D.J. Bacon, J. Nucl. Mater. 223 (1995) 245.